Buoyancy Arrest and Bottom Ekman Transport. Part II: Oscillating Flow

K. H. BRINK AND S. J. LENTZ

Department of Physical Oceanography, Woods Hole Oceanographic Institution, Woods Hole, Massachusetts

ABSTRACT

The effects of a sloping bottom and stratification on a turbulent bottom boundary layer are investigated for cases where the interior flow oscillates monochromatically with frequency ω. At higher frequencies, or small slope Burger numbers $s = \alpha N/f$ (where α is the bottom slope, N is the interior buoyancy frequency, and f is the Coriolis parameter), the bottom boundary layer is well mixed and the bottom stress is nearly what it would be over a flat bottom. For lower frequencies, or larger slope Burger number, the bottom boundary layer consists of a thick, weakly stratified outer layer and a thinner, more strongly stratified inner layer. Approximate expressions are derived for the different boundary layer thicknesses as functions of s and $\sigma = \omega/f$. Further, buoyancy arrest causes the amplitude of the fluctuating bottom stress to decrease with decreasing σ (the s dependence, although important, is more complicated). For typical oceanic parameters, arrest is unimportant for fluctuation periods shorter than a few days. Substantial positive (toward the right when looking toward deeper water in the Northern Hemisphere) time-mean flows develop within the well-mixed boundary layer, and negative mean flows exist in the weakly stratified outer boundary layer for lower frequencies and larger s. If the interior flow is realistically broad band in frequency, the numerical model predicts stress reduction over all frequencies because of the nonlinearity associated with a quadratic bottom stress. It appears that the present one-dimensional model is reliable only for time scales less than the advective time scale that governs interior stratification.

1. Introduction

Over a sloping bottom, steady along-isobath-interior flow gives rise to a near-bottom cross-isobath Ekman transport and, if stratification is present, produces cross-isobath density gradients. These gradients, through a thermal wind balance, ultimately bring the bottom velocity and bottom stress to zero. This general problem was addressed by Weatherly and Martin (1978, hereafter WM78) and then subsequently by numerous other authors (e.g., MacCready and Rhines 1991; Trowbridge and Lentz 1991; MacCready and Rhines 1993; Garrett et al. 1993; Ramsden 1995a,b; Middleton and Ramsden 1996, hereafter MR96; Romanou and Weatherly 2001, 2004; Brink and Lentz 2010, hereafter Part I). Up until Ramsden (1995b), effort was concentrated mainly on initial-value problems where an along-isobath interior flow is suddenly imposed. Since then, a few authors (e.g.,

MR96; Romanou and Weatherly 2004) considered the bottom boundary layer response to time-dependent (oscillating) interior flow. There are substantial asymmetries in the initial-value problem, whereby upwelling bottom Ekman transports are associated with thin (relative to the flat-bottom case), highly stable boundary layers and with rapid adjustment, whereas downwelling Ekman transport causes gravitational instabilities and hence deeper boundary layers and slower adjustment (Fig. 1). Because thinner boundary layers require less total cross-isobath volume transport to reach geostrophic equilibrium, the difference in time scales makes physical sense. In either case, the steady-state boundary layer is always stably stratified, and fairly simple analytical expressions exist to describe the layer thickness (Part I). Because of the upwelling–downwelling asymmetries, one might expect some potentially interesting effects in an oscillating problem where flow passes alternatively from one direction to the other.

Boundary layer arrest is important for a number of reasons. For example, Chapman and Lentz (1994) and Chapman (2000b) showed how physics related to the buoyancy arrest mechanism determine the cross-shelf
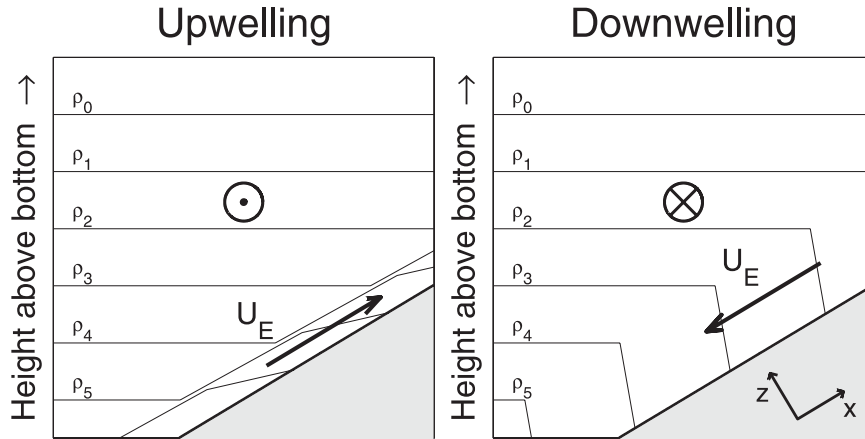

Upwelling   Downwelling

FIG. 1. Schematic of bottom boundary layer processes in the case of a steady interior flow, where U_E is the bottom Ekman transport before buoyancy arrest is complete. The contours represent the density field after arrest is complete. Shown are the cases of (left) negative (upwelling favorable) and (right) positive (downwelling favorable) along-isobath velocity.

locations of surface-to-bottom fronts in the coastal ocean. Further, Chapman and Lentz (1994) and Chapman (2000a) show how the absence of bottom stress in an adjusted current greatly extends the alongshore scale of an along-isobath current. It is not obvious how these results, derived for a nearly steady flow, might be affected by the presence of a fluctuating flow. In addition, there are long-standing questions about the extent to which buoyancy arrest mitigates the frictional damping experienced by time-dependent flows such as coastal trapped waves in the "weather band" of 2–10-day time scales. It is intuitive, given the finite adjustment time scales, that there should be frequency ranges where arrest is or is not important.

Thus, we treat buoyancy arrest in the case where the interior flow is time dependent. This problem has been explored to some extent in the literature (e.g., Ramsden 1995b; MR96; Romanou and Weatherly 2004), but we attempt here to take a somewhat more systematic approach to the problem. Our ultimate goal is to reach a level of understanding that can be applied to the real ocean, where there is a continuous temporal spectrum of variability and where lateral variations allow density advection above the bottom boundary layer. To reach this goal, the problem must be broken into an orderly progression of steps. The first task, undertaken here, is to treat the case of an oscillating interior flow in the classical one-dimensional context. This simple problem allows an understanding of how boundary layer properties (structure, degree of arrest, and flow rectification) depend on the key parameters, such as stratification and forcing frequency (section 4). A necessary preliminary for this problem is to review and encapsulate results for an oscillating flow over a flat bottom (section 3). In approaching both of these tasks, results are consistently summarized in terms of boundary layer thicknesses and bottom stress.

2. Model formulation

Following WM78, for example, the equations of motion are rotated into a coordinate system where axes are either parallel or perpendicular (z) to the bottom. The interior velocity (u_I, v_I) is constant with height, and the initial interior density $\rho_I = \rho_0 + \rho_{Iz}z$ varies linearly in the vertical. Under these conditions, the equations governing boundary layer quantities are

$$u_{Et} - fv_E = -g\alpha\rho_E/\rho_0 + (Au_{Ez})_z, \qquad (1a)$$

$$v_{Et} + fu_E = (Av_{Ez})_z, \quad \text{and} \qquad (1b)$$

$$\rho_{Et} + u_E\alpha\rho_{Iz} = (K\rho_{Ez})_z, \qquad (1c)$$

and the interior density is governed by

$$\rho_{It} + u_I\alpha\rho_{Iz} = (K\rho_{Iz})_z. \qquad (1d)$$

Subscripts with regard to an independent variable indicate partial differentiation; A and K are an eddy viscosity and eddy diffusivity, respectively; and u_E, v_E, and ρ_E are boundary layer cross-isobath velocity, along-isobath velocity, and density, respectively (where, e.g., the total along-isobath velocity $v = v_I + v_E$). All boundary layer variables vanish far from the bottom. The Coriolis parameter is f, α is the (constant, small) bottom slope, and g is the acceleration due to gravity. For all cases given here, $\alpha \geq 0$; therefore, upslope flow corresponds to $u > 0$. In the interior (well above the bottom boundary layer), diffusion is very slow, so the buoyancy frequency squared

is effectively constant at $N^2 = -g\rho_{Iz}/\rho_0$. This formulation reduces a physically two-dimensional problem to a one-dimensional system that varies spatially only in the rotated vertical direction. The Burger number and frictional parameter,

$$s = \frac{\alpha N}{f} \quad \text{and} \quad d = \frac{c_D N}{f} \qquad \text{(2a, b)}$$

(where c_D is the bottom drag coefficient), respectively, are both frequently used nondimensional numbers in this analysis (e.g., Trowbridge and Lentz 1991).

Solutions to (1) are matched to a logarithmic layer at height $z = z_T$ above the physical bottom:

$$A u_{Ez} = c_D [(u_I + u_E)^2 + (v_I + v_E)^2]^{1/2} (u_I + u_E) \quad \text{and} \qquad \text{(3a)}$$

$$A v_{Ez} = c_D [(u_I + u_E)^2 + (v_I + v_E)^2]^{1/2} (v_I + v_E), \quad \text{where} \qquad \text{(3b)}$$

$$c_D = \left[\frac{\kappa}{\ln(z_T/z_0)} \right]^2. \qquad \text{(3c)}$$

The bottom roughness is described by z_0, and $\kappa = 0.4$ is von Kármán's constant.

The interior flow is given as

$$u_I = 0, \quad v_I = v_0 \sin(\omega t), \qquad \text{(4a, b)}$$

and the normalized frequency $\sigma = \omega/f$ is a third important nondimensional parameter in the problem. The restrictive form (4) for the time-dependent interior flow requires a specific combination (analogous to a Kelvin wave) of spatially uniform x and y pressure gradients. An alternative approach is to set v_I and require no along-isobath pressure gradient, so that $u_I \neq 0$, and the overall interior flow amplitude varies with frequency. This would complicate interpretation a good deal. Other boundary conditions are that there is no density flux through the bottom and that $(A u_{Ez})_z = (A v_{Ez})_z = (K\rho_z)_z = 0$ at the top of the numerical grid (normally $z = 60$ m but higher if required). These conditions maintain a linear interior density profile and yield no turbulent stress at the upper boundary (Part I).

The system (1) is solved numerically using implicit time stepping on a vertically uniform 20-cm grid (Part I). The advantage of the constant grid spacing is that it allows resolution of the sharp density or velocity jumps that can occur across the top of the bottom boundary layer. The Mellor–Yamada 2.5 turbulence closure scheme is used throughout the following unless otherwise noted. A sampling of runs was repeated with Mellor–Yamada 2.0 and with k–ε schemes, and there were quantitative differences

(typically less than 20% in boundary layer thickness) but no qualitative differences in the results. All schemes are implemented following Wijesekera et al. (2003).

3. Flat bottom with time dependence

a. Analysis

Oscillating flow above a flat bottom ($\alpha = s = 0$) provides an important context for the more complex problem over a sloping bottom. Consider a flat-bottom ocean, with a slab-like bottom boundary layer of thickness h. In this case, the layer-integrated equations of motion are

$$U_{Et} - f V_E = -r U_E \quad \text{and} \qquad \text{(5a)}$$

$$V_{Et} + f U_E = -r V_E - \rho_0^{-1} \langle \tau^y \rangle e^{i\omega t}, \qquad \text{(5b)}$$

where U_E and V_E are transports (depth-integrated boundary layer velocities), $\langle \tau^y \rangle$ is the amplitude of the bottom stress associated with the interior flow ($\langle \xi \rangle$ denotes the amplitude of a fluctuating quantity ξ), and r describes a Raleigh friction associated with bottom friction acting on the boundary layer component of flow [the more intuitive form, stress proportional to velocity (e.g., U_E/h), does not perform any better]. Then,

$$U_E = \langle U_E \rangle e^{i\omega t}, \quad V_E = \langle V_E \rangle e^{i\omega t} \qquad \text{(6b, c)}$$

and, from (5),

$$\langle U_E \rangle = -\frac{f \rho_0^{-1} \langle \tau^y \rangle}{(f^2 - \omega'^2)},$$

$$\langle V_E \rangle = -\frac{i\omega' \rho_0^{-1} \langle \tau^y \rangle}{(f^2 - \omega'^2)}, \qquad \text{(7a, b)}$$

where $\omega' = \omega - ir$.

The problem is closed by assuming that the boundary layer thickness is consistent with the bulk Richardson number being constant at a critical value of R_b. The associated velocity and density jumps across the top of the layer are δv and $\delta\rho$. A representative shear across the top of the layer is then given, using (7), by

$$|\delta v|^2 = \rho_0^{-2} h^{-2} \left| [(f \langle \tau^y \rangle)^2 + (\omega' \langle \tau^y \rangle)^2] (f^2 - \omega'^2)^{-2} \right|. \qquad \text{(8)}$$

Assuming that the initial stratification is given by $\rho = \rho_0 + \rho_{Iz} z$, the density difference resulting from entrainment across the top of the bottom mixed layer is $\delta\rho = -\rho_{Iz} h/2$. Thus, the bulk Richardson number for the bottom boundary layer is

$$R_b = \frac{gh\delta\rho}{(\rho_0 |\delta v|^2)}$$

$$= 0.5 N^2 h^4 \langle u^* \rangle^{-4} \left| (f^2 - \omega'^2)^2 (f^2 + \omega'^2)^{-1} \right|, \qquad \text{(9)}$$

where $u*$ is the friction velocity and $\langle u* \rangle^2 = \langle \tau^y \rangle / \rho_0$. Equation (9) is solved for h to obtain

$$h^F = \langle u* \rangle (2R_b)^{1/4} |f^2 + \omega'^2|^{1/4} |f^2 - \omega'^2|^{1/2} N^{-1/2}. \quad (10)$$

The superscript F is used to identify this as the boundary layer thickness over a flat bottom. Expression (10) can be expanded for $r \ll \omega$ to obtain

$$h^F = \langle u* \rangle c |f^2 + \omega^2|^{1/4} |(f^2 - \omega^2)^2 + 4r^2\omega^2|^{-1/4} N^{-1/2}, \quad (11)$$

where $c = (2R_b)^{1/4}$. Inclusion of the weak bottom stress acting on the boundary layer (as opposed to interior) flow avoids a singularity that would otherwise occur at $\omega = \pm f$.

The boundary layer thickness (11) with steady conditions and $r = 0$ becomes

$$h_0^F \approx \langle u* \rangle c (Nf)^{-1/2}, \quad (12)$$

analogous to the Pollard Rhines and Thompson (1973) depth for the ocean surface mixed layer (Thompson 1973). WM78 have a similar expression, but replace N by $(f^2 + N^2)^{1/2}$, a negligible difference under most stratified conditions. Expression (13) agrees quantitatively with the WM78 result if $c = (2R_b)^{1/4} = 1.3$ (see section 3b).

It is necessary to relate the interior velocity v_I to the bottom stress. WM78, in their steady problem, use $u* = b_1 c_D^{1/2} v_I$, where b_1 is an empirical constant. Although this expression is a reasonable starting point, it must be modified to account for time dependence. Specifically, there is a decrease in the bottom stress (for a fixed v_I amplitude) near the inertial frequency (as can be seen by considering the time-dependent boundary layer equations with a constant eddy viscosity A_0). This near-inertial behavior is treated empirically here by modifying the assumed velocity–stress relation to

$$\langle u* \rangle^F = b_1 c_D^{1/2} v_0 F(\omega) \quad \text{and} \quad (13a)$$

$$F(\omega) = \frac{1}{2}(2 - e^{-\lambda|f+\omega|/f} - e^{-\lambda|f-\omega|/f}), \quad (13b)$$

where λ is an empirical constant.

b. Calculations

A sequence of 28 flat-bottom, numerical model experiments was conducted, and these included variations in stratification, Coriolis parameter, bottom roughness, interior flow amplitude, and forcing period (Table 1). In each case, the model uses strictly oscillating interior flow, starting from rest and uses Mellor–Yamada level 2.5 turbulence closure. The model is run for 25 days, and

TABLE 1. Summary of flat-bottom model runs.

Run No.	$N^2 \times 10^4$ (s^{-2})	$f \times 10^4$ (s^{-1})	v_0 (cm s^{-1})	Period (h)	z_0 (cm)	h_q (m)
1	0.95	1.00	20	12.42	0.03	17.1
2	0.95	1.00	30	12.42	0.03	24.8
3	0.95	1.00	40	12.42	0.03	32.7
4	0.95	1.00	10	12.42	0.03	9.1
5	0.95	0.63	15	12.42	0.03	10.3
6	0.00	1.00	20	12.42	0.03	55.8
7	0.04	1.00	20	12.42	0.03	37.8
8	0.19	1.00	20	12.42	0.03	26.5
9	4.76	1.00	20	12.42	0.03	10.5
10	0.95	0.10	20	12.42	0.03	15.1
11	0.95	0.50	20	12.42	0.03	15.3
12	0.95	1.00	20	6.00	0.03	14.1
12a	0.95	1.00	20	8.73	0.03	14.7
12b	0.95	1.00	20	13.96	0.00	18.1
12c	0.95	1.00	20	17.45	0.03	13.7
12d	0.95	1.00	20	15.58	0.03	19.3
13	0.95	1.00	20	18.00	0.03	21.4
13a	0.95	1.00	20	20.53	0.03	20.1
14	0.95	1.00	20	24.00	0.03	19.3
15	0.95	1.00	20	30.00	0.03	18.1
16	0.95	1.00	20	36.00	0.03	17.7
17	0.95	1.00	20	48.00	0.03	17.5
18	0.95	1.00	20	72.00	0.03	17.5
19	0.95	1.00	20	20.00	0.03	16.7
20	0.95	1.00	20	192.00	0.03	17.1
21	0.95	1.00	20	288.00	0.03	17.2
22	0.95	1.00	20	12.42	0.02	16.5
23	0.95	1.00	20	12.42	0.04	17.3

the boundary layer thickness is determined (following WM78) as h_q, the height at which turbulent kinetic energy, averaged over a period, goes to zero. A more traditional alternative boundary layer definition is the height at which the vertical density gradient is a maximum h_ρ (location of the density "cap"), and this is the same as h_q (to within a few tenths of a meter) over a flat bottom. This maximum gradient definition becomes problematic, however, when (as in the steady downwelling problem over a sloping bottom; Part I) there is not an obvious sharp cap. In much of the following, we will use yet another boundary layer definition, $h_{\rho\rho}$, the height above the bottom where the period-averaged second derivative of density ρ_{zz} reaches a positive extremum. When the boundary layer has a sharp density cap, $h_{\rho\rho}$ is virtually identical to h_ρ, the thickness defined by the maximum density gradient. When the boundary layer structure is smoother (as in the "smooth" upwelling case in Part I), the $h_{\rho\rho}$ definition selects the height at which the boundary layer transitions from a strongly stratified lower region to a weakly stratified upper region. In the following, the turbulence h_q and second-derivative $h_{\rho\rho}$ definitions are used exclusively. The numerical boundary layer thickness is always computed using variables (density or
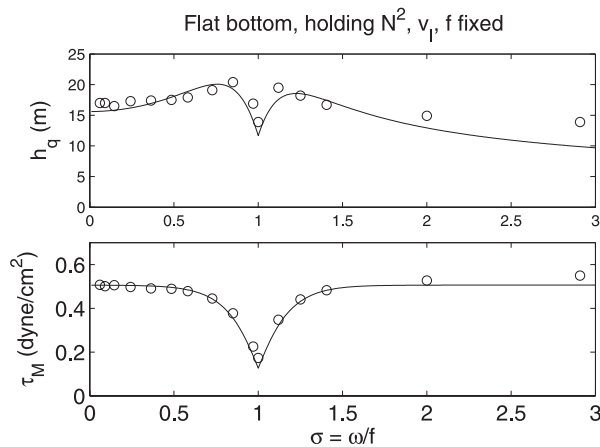
FIG. 2. Flat-bottom results: (top) boundary layer thickness and (bottom) major-axis bottom stress amplitude as a function of normalized frequency with N^2, v_0, and f all held constant at 1×10^{-4} s^{-2}, 20 cm s^{-1}, and 1×10^{-4} s^{-1}, respectively. The solid lines are the functional fits using (11) and (13).

turbulence kinetic energy) averaged over the last full forcing period. Because the boundary layer thickness varies only slowly for times greater than 10–20 days, this approach does not "smear" the profile badly, and it does average out any intermittency. It might seem more natural to estimate the boundary layer thickness instantaneously, but we found in some cases (e.g., h_q for Fig. 6c) that this leads to considerable variability and ambiguity. We find that the turbulence-based estimate h_q for the period average equals the maximum instantaneous h_q over that period. The density-based estimate $h_{\rho\rho}$ averaged over a period is less intermittent, and the period-averaged value is typically near the mode of the instantaneous values. For a sharply capped boundary layer, as is found with a flat bottom, averaging layer thickness makes little difference after the first inertial period.

Numerical model results are used to evaluate the scalings and to calculate the empirical coefficients by minimizing rms error. Specifically, $b_1 = 0.65$ and $\lambda = 7.5$ by fitting (13), and $r^2 = 1 \times 10^{-9}$ s^{-2} and $c = 2.2$ by fitting (11). The resulting rms error in the $\langle u* \rangle^F$ estimate (scaling versus numerical results) is 0.035 cm s^{-1} and the correlation is 0.99. In the fit for h_q, the rms error is 1.5 m and the correlation 0.99. The expressions (11) and (13) reasonably approximate the near-inertial peak in layer thickness and reduction in bottom stress, respectively (Fig. 2).

In the limit of zero frequency, (12) is expected to agree with the WM78 results. Indeed, the form is essentially the same, but WM78 obtain $c = 1.3$ instead of the present 2.2. This difference is investigated through a series of model runs. For an initial-value problem with steady interior flow, the exact WM78 results were reproduced with a logarithmically stretched grid, Mellor–Yamada 2.0

closure and a five-day run length. Three things about the present calculations differ from WM78. First, WM78 used a vertically stretched grid that has relatively coarse resolution (100 cm) away from the bottom (although their near-bottom resolution was 1 cm). All else being the same, the present uniformly fine grid leads to a typical increase in calculated h_q of about 15%–25%. Second, WM78 used Mellor–Yamada 2.0 closure, but Mellor–Yamada 2.5 is used here; this typically increases the boundary layer thickness by about 30% for the steady problem (e.g., Part I, appendix). Finally, WM78 seem to have typically run their model for about 5 days versus the present 25 days. Longer runs allow slow thickening after the half first inertial period, hence a typical increase in layer thickness of about 15% over the additional 20 days (so that c is actually weakly time dependent). These three differences in model usage all work to increase h_q and together account for the difference between $c = 1.3$ and $c = 2.2$.

4. The oscillating sloping bottom model

a. Overview of numerical results

To gain an initial appreciation of the problem, we first describe a sampling of results from a sequence of 53 numerical model runs (Table 2) that include variations in bottom slope, stratification, bottom roughness, Coriolis parameter, and the amplitude and frequency of interior flow.

First, consider boundary layer thickness as a function of s for numerical runs with a fixed 4-day v_I period (Fig. 3, top). There are two boundary layer structure regimes in this case. For smaller s (<0.3), the two boundary layer depth definitions (h_q and $h_{\rho\rho}$) are virtually identical because there is a bottom mixed layer with a sharp density cap at its top (Fig. 4, solid line). The thickness values indeed approach the expected flat-bottom value [Eq. (11)] of 17 m as $s \to 0$. As s increases toward $s = 0.3$, the boundary layer (by either definition) becomes thinner, as might be expected (e.g., MR96; Part I) in the steady capped upwelling case when the bottom slope or stratification increases (s increases). In this regime of weak bottom slope, the downward cross-isobath density transport in the bottom boundary layer [which is proportional to Ekman velocity times sN/σ in (1c)] is never strong enough to destabilize the layer. That is to say that the density contrast associated with entrainment across the top of the layer (Fig. 5a) is always strong enough to counteract destabilization by downslope Ekman transport. The fluctuating cross-isobath flow is relatively symmetric (Fig. 5b); it has about the same amplitude and vertical structure during both the upwelling (positive; days 2–4, 6–8, and 10–12) and downwelling phases.

TABLE 2. Summary of sloping-bottom oscillating runs.

Run No.	$N^2 \times 10^4$ (s^{-2})	$f \times 10^4$ (s^{-1})	v_0 (cm s^{-1})	Period (days)	z_0 (cm)	α	h_q (m)	$h_{\rho\rho}$ (m)	s
40	0.95	1.00	20	4.00	0.03	0	17.1	17.1	0
41	0.95	1.00	20	4.00	0.03	0.0005	17.3	17.5	0.05
42	0.95	1.00	20	4.00	0.03	0.0010	16.3	16.5	0.10
42.5	0.95	1.00	20	4.00	0.03	0.0018	14.7	14.9	0.18
43	0.95	1.00	20	4.00	0.03	0.0025	13.1	13.3	0.24
43.5	0.95	1.00	20	4.00	0.03	0.0037	17.0	8.9	0.36
44	0.95	1.00	20	4.00	0.03	0.0050	18.3	7.9	0.49
44.25	0.95	1.00	20	4.00	0.03	0.0062	21.2	7.5	0.60
44.5	0.95	1.00	20	4.00	0.03	0.0075	22.4	7.9	0.73
46	0.95	1.00	20	4.00	0.03	0.0100	23.0	7.7	0.98
46.25	0.95	1.00	20	4.00	0.03	0.0125	22.1	7.3	1.22
46a	0.95	1.00	20	4.00	0.03	0.0150	22.2	4.7	1.46
46.75	0.95	1.00	20	4.00	0.03	0.0175	21.4	7.5	1.71
49	0.95	1.00	20	2.00	0.03	0.0050	13.4	8.7	0.49
50	0.95	1.00	20	8.00	0.03	0.0050	27.1	7.9	0.49
51	0.95	1.00	20	8.00	0.03	0.0025	19.7	9.5	0.24
52	0.95	1.00	−20	8.00	0.03	0.0025	17.5	9.5	0.24
53	0.48	1.00	20	8.00	0.03	0.0025	21.1	13.1	0.17
54	0.95	1.00	30	8.00	0.03	0.0025	29.3	13.7	0.24
55	0.95	1.00	−30	8.00	0.03	0.0025	24.9	13.5	0.24
56	0.95	1.00	30	8.00	0.03	0.0050	38.4	11.3	0.49
57	0.95	1.00	−30	8.00	0.03	0.0050	38.5	11.3	0.49
58	0.95	0.50	30	8.00	0.03	0.0050	34.5	12.7	0.98
59	0.95	1.00	30	8.00	0.03	0.0100	38.3	9.3	0.98
60	0.48	1.00	30	8.00	0.03	0.0050	40.3	13.9	0.34
61	0.95	1.00	20	2.00	0.03	0.0050	14.0	8.7	0.49
62	0.95	1.00	−20	2.00	0.03	0.0050	13.0	8.7	0.49
63	0.95	1.00	20	1.50	0.03	0.0050	13.6	13.7	0.49
64	0.95	1.00	20	1.00	0.03	0.0050	13.5	13.3	0.49
65	0.95	1.00	20	0.75	0.03	0.0050	16.2	16.1	0.49
66	0.95	1.00	20	0.50	0.03	0.0050	14.9	14.7	0.49
66.25	0.95	1.00	20	0.37	0.03	0.0050	10.3	10.7	0.49
66.5	0.95	1.00	20	0.58	0.03	0.0050	18.2	18.3	0.49
66.75	0.95	1.00	20	0.65	0.03	0.0050	14.1	14.1	0.49
67	0.95	1.00	20	0.25	0.03	0.0050	9.0	9.3	0.49
67.25	0.95	1.00	20	8.00	0.03	0.0050	27.2	7.9	0.49
67.5	0.95	1.00	20	12.00	0.03	0.0050	29.8	7.1	0.49
67.75	0.95	1.00	20	0.30	0.03	0.0050	9.5	9.7	0.49
68	0.95	1.00	20	0.60	0.03	0.0100	13.7	13.7	0.98
69	0.95	1.00	20	0.40	0.03	0.0100	12.8	12.7	0.98
70	0.95	1.00	20	0.80	0.03	0.0100	11.0	7.3	0.98
71	0.95	1.00	−20	4.00	0.03	0.0050	18.5	7.9	0.49
72	0.95	1.00	50	0.52	0.03	0.0050	36.1	36.1	0.49
73	0.95	0.50	20	8.00	0.03	0.0100	20.2	8.1	1.95
74	0.48	0.50	20	8.00	0.03	0.0050	30.7	12.1	0.69
75	1.90	1.00	10	8.00	0.03	0.0100	10.1	12.9	1.38
76	2.85	1.00	15	8.00	0.03	0.0150	11.0	4.5	2.53
77	1.90	0.50	15	8.00	0.03	0.0100	10.0	5.1	2.76
78	1.64	0.63	30	8.00	0.03	0.0100	25.2	9.5	2.03
79.25	0.95	1.00	20	0.73	0.03	0.0150	11.7	6.7	1.46
79.5	0.95	1.00	20	0.48	0.03	0.0150	11.3	6.9	1.46
401	4.76	1.00	20	8.00	0.03	0.0150	11.5	4.7	3.27
402	5.71	1.00	20	10.00	0.03	0.0200	9.5	8.5	4.79

Some asymmetry between phases is obvious in the eddy viscosity (Fig. 5c; taken here as a measure of boundary layer turbulence), in that the eddy viscosity is larger and extends farther upward during the downwelling ($u < 0$) phase, as might be expected, given the decreased stratification (Fig. 5a) during this phase. This regime with an overall sharply defined boundary layer, where h_q and $h_{\rho\rho}$ are virtually equal, is henceforth called the capped
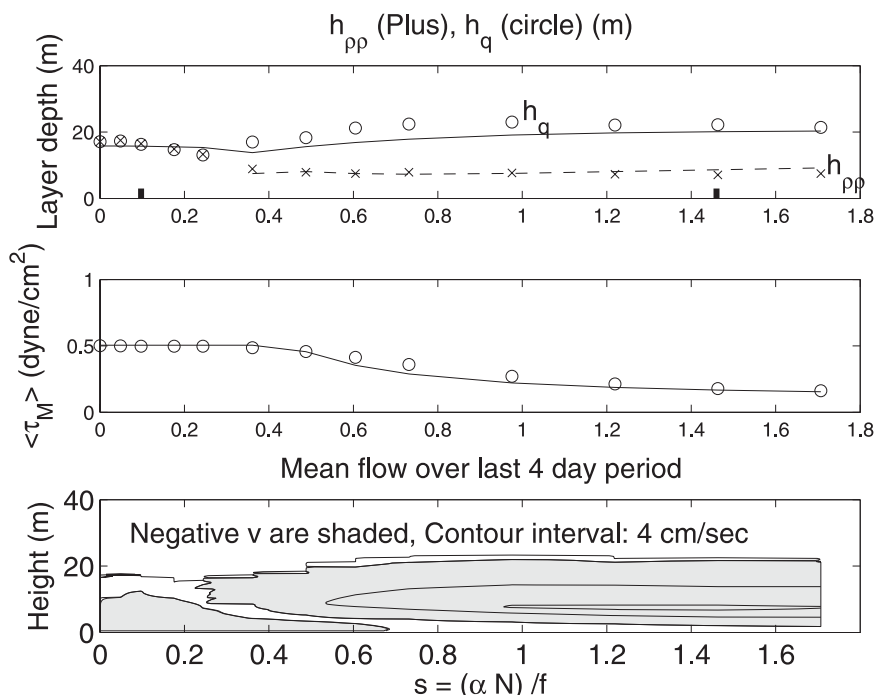
FIG. 3. Summary plot of model runs with a constant forcing period of 4 days ($\sigma = 0.18$), $v_0 = 20$ cm s^{-1}, and varying s: (top) h_q (circles) and $h_{\rho\rho}$ ($\times$). Solid lines represent analytical expressions (19) (capped regime) or (23) (divided regime) for the outer boundary layer thickness. The dashed line is the analytical expression h^i for $h_{\rho\rho}$ [in (30a)]. (middle) Amplitude of the computed major axis of bottom stress (circles) and analytical expression (36), equating $\langle u^{*A} \rangle^2$ to major-axis stress amplitude, and (bottom) mean along-isobath velocity contoured as a function of height and s are shown. Negative values are shaded, and the contour interval is 4 cm s^{-1}.

regime. For comparison, the Perlin et al. (2005) measurements are apparently made in a capped regime, and they also observe enhanced turbulence during downwelling.

At larger s (>0.3 in Fig. 3), the boundary layer structure is distinctly different in that h_q and $h_{\rho\rho}$ diverge for mean conditions. There is an inner, more strongly stratified region with thickness $h_{\rho\rho}$ and an outer, weakly stratified region (identified with h_q) that is still somewhat turbulent and that joins smoothly to the interior (Fig. 4, dashed line). The difference between h_q and $h_{\rho\rho}$ grows as s increases over the range of $0.3 < s < 1$, but the difference decreases slightly for larger s. The inner boundary layer (Figs. 6a,b) increases from zero thickness at the start of the upwelling phase of each cycle, is relatively constant for an interval, and then briefly vanishes late in the downwelling phase. As MR96 (see their Fig. 9) point out for their calculation in this parameter range, a constant, steady shear sets up quickly in the outer boundary layer (Fig. 4, right, shows its mean), and we find its magnitude to be consistent with the time-mean along-isobath flow in the outer layer being geostrophically balanced. Effectively, the outer boundary layer flow is

a sum of the oscillating interior flow plus a steady, uniformly sheared, geostrophically balanced mean flow (between 8 and 20 m in Fig. 4, dashed line). The physical situation is clarified by Figs. 6a,b. After the first cycle, downwelling (e.g., days 4–6, 8–10, etc.) flow is weak but associated with a thickening layer. During the upwelling phase (e.g., days 6–8, etc.), the boundary layer flow is stronger and more concentrated near the bottom. Eddy viscosity in the inner boundary layer (Fig. 6c) is smaller than in the capped regime (about 20 cm^2 s^{-1} maximum versus 100 cm^2 s^{-1} in Fig. 5c for these two examples) and confined to the bottom 5 m. Above this depth range of obvious Ekman transport, at heights 8–20 m above the bottom, the main u features (Fig. 6b) are oscillations, grading slightly in phase vertically, with a period of about 0.39 days (compared to the inertial period of 0.72 days). These oscillations are also very evident in the eddy viscosity (Fig. 6c), where, once per cycle, there is a burst of turbulence that lasts about 0.05 days [these bursts show as nearly vertical streaks for 8 m $< z <$ 20 m in (6c)]. At other times, turbulence is negligible in the outer part of the boundary layer. Steady downwelling initial-value
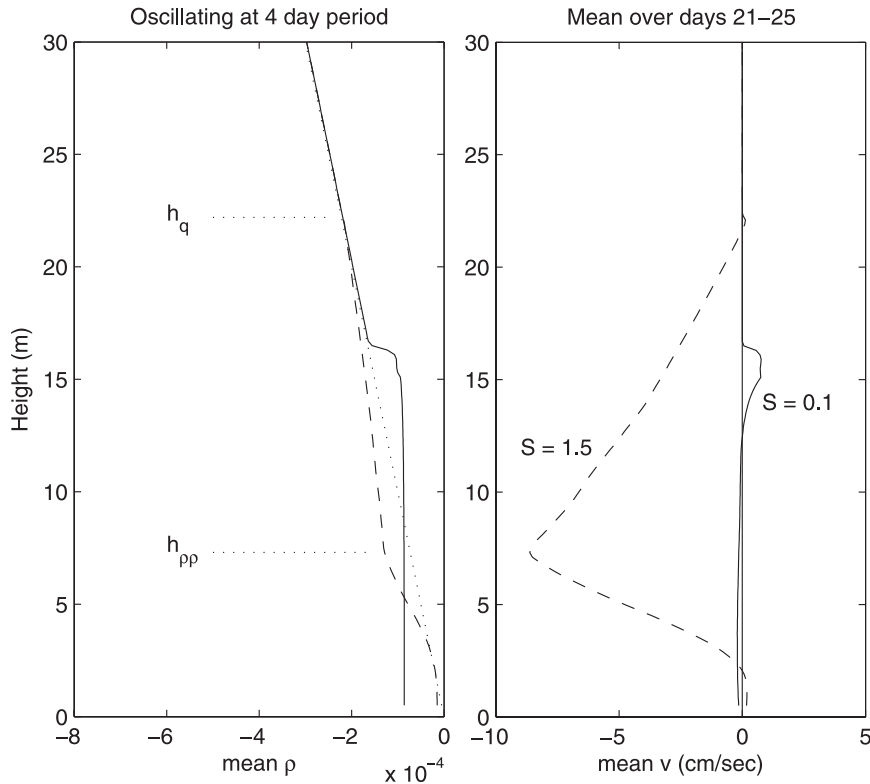
FIG. 4. (left) Mean (over the last 4-day forcing cycle) density and (right) total along-isobath velocity for runs with $v_0 = 20$ cm s^{-1} and $s = 0.1$ (run 42: solid curves, having a distinct cap in the density) or $s = 1.5$ (run 46a: dashed curves). These runs are indicated by solid vertical bars in Fig. 3. The layer depths h_q (height of no mixing) and $h_{\rho\rho}$ (height of maximum density second derivative) are labeled for the $s = 1.5$ (dashed line) case. The dotted line indicates the initial density profile.

numerical experiments with larger s also show these boundary layer oscillations (Part I). The oscillating boundary layer regime where there are distinct inner and outer boundary layers (h_q and $h_{\rho\rho}$ diverge) is called the "divided" regime. For comparison, the time-dependent runs in MR96 appear to be in the divided regime, whereas those of Romanou and Weatherly (2004) are in both the capped and divided regimes.

It is only in this divided regime that the bottom stress begins to decrease noticeably with s (Fig. 3, middle), as might be expected when buoyancy arrest is effective. The time series of bottom stress (not shown) always remain essentially symmetric between upwelling and downwelling phases, so the mean bottom stress is always small (less that about 0.02 dyne cm^{-2}) for all runs. A substantial mean flow develops nonetheless (Fig. 3, bottom), and this is treated in section 4g.

Another way to view the model results is to hold s constant at 0.5 and to vary the nondimensional frequency $\sigma = \omega/f$ (Fig. 7). Again, the two different boundary layer

structural regimes are found. As frequency approaches zero, the boundary layer is divided, the bottom stress amplitude decreases, and a substantial mean flow (< -6 cm s^{-1}) develops in the outer boundary layer. At higher frequencies, the boundary layer is capped, the cross-shelf Ekman transport excursions become smaller, and buoyancy arrest ceases to be important. For $\sigma > 0.5$, the results closely resemble those in the flat-bottom case in that h_q and $h_{\rho\rho}$ become identical and the stress decreases markedly near the effective inertial frequency $\omega = f^* > f$. This shift can be readily justified by considering the governing Eq. (1) in the absence of eddy viscosity, so that free oscillations are found for

$$\omega^2 = f^2 + \alpha^2 N^2 = f^2(1 + s^2) \equiv f^{*2}. \qquad (14)$$

These motions, noted previously by MR96, are essentially internal gravity waves with their crests parallel to the bottom. Very often, in calculations such as those in
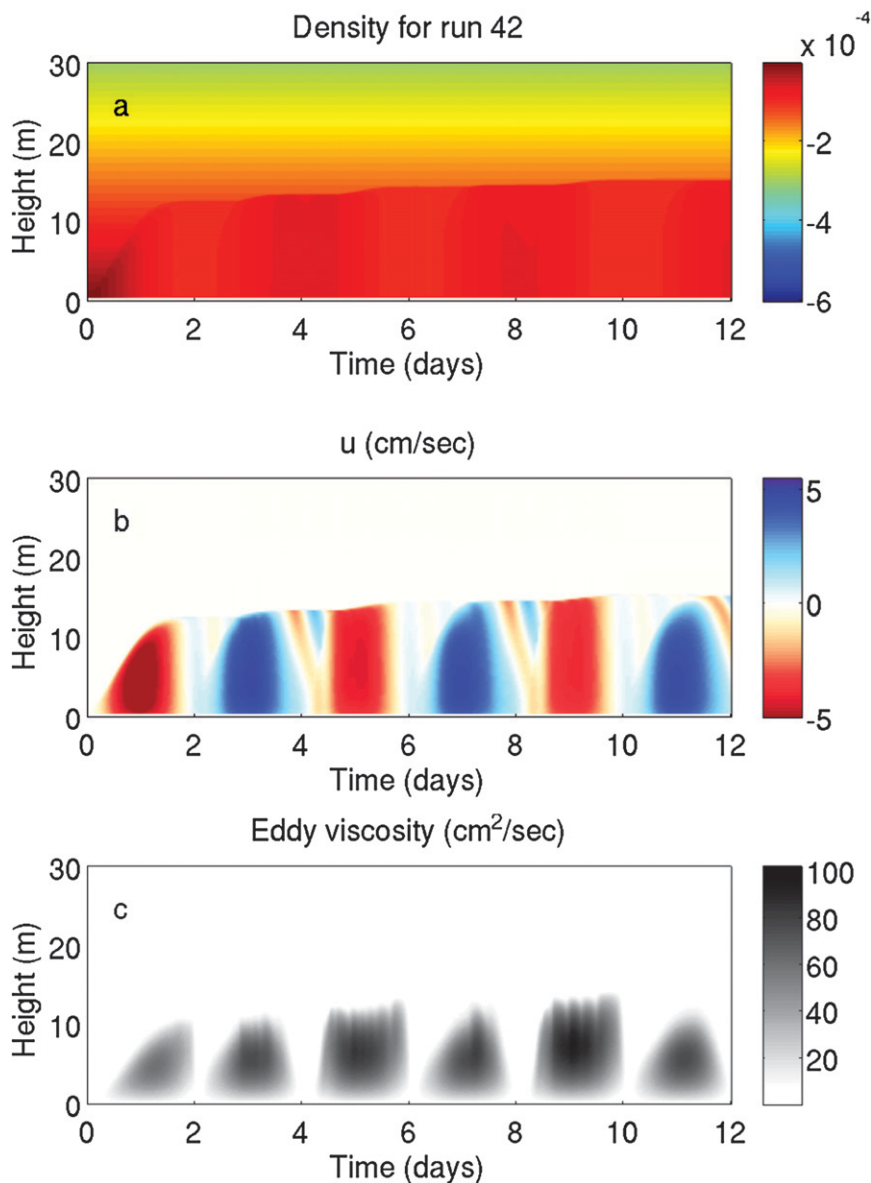
FIG. 5. Results from model run 42 (4-day period, $s = 0.1$ and $v_0 = 20$ cm s^{-1}) as a function of height and time: (a) density (gm cm^{-3}), (b) cross-isobath currents (cm s^{-1}), and (c) model eddy viscosity (cm^2 s^{-1}). For clarity, only the first 12 days of the run are shown.

Fig. 6 (where f^* for $s = 1.5$ corresponds to a period of 0.40 days), the oscillations occur at a frequency slightly higher than f^* and the oscillations have a vertical phase gradient (tilt in Fig. 6) inconsistent with the derivation of (14). This can be rationalized by considering (1) with a constant, uniform eddy viscosity: vertical phase variations and higher frequencies become possible. Given, however, the extremely intermittent eddy viscosity when these "buoyancy oscillations" are present in model runs (e.g., Fig. 6c), it is clear that a constant eddy viscosity rationalization is suggestive at best.

To quantify phenomenology in the boundary layer beneath oscillating interior flow, we parameterize the boundary layer thicknesses (both h_q and h_{pp}) as a function of the important nondimensional parameters s, d, and σ for the three cases: capped regime, divided regime outer, and divided regime inner (sections 4b–d). A criterion is then developed to define when the capped and divided regimes should prevail (section 4e). Once the expressions for the boundary layer thicknesses are found, the bottom stress arrest is treated (section 4f) and the inherent rectified flows are described (section 4g).
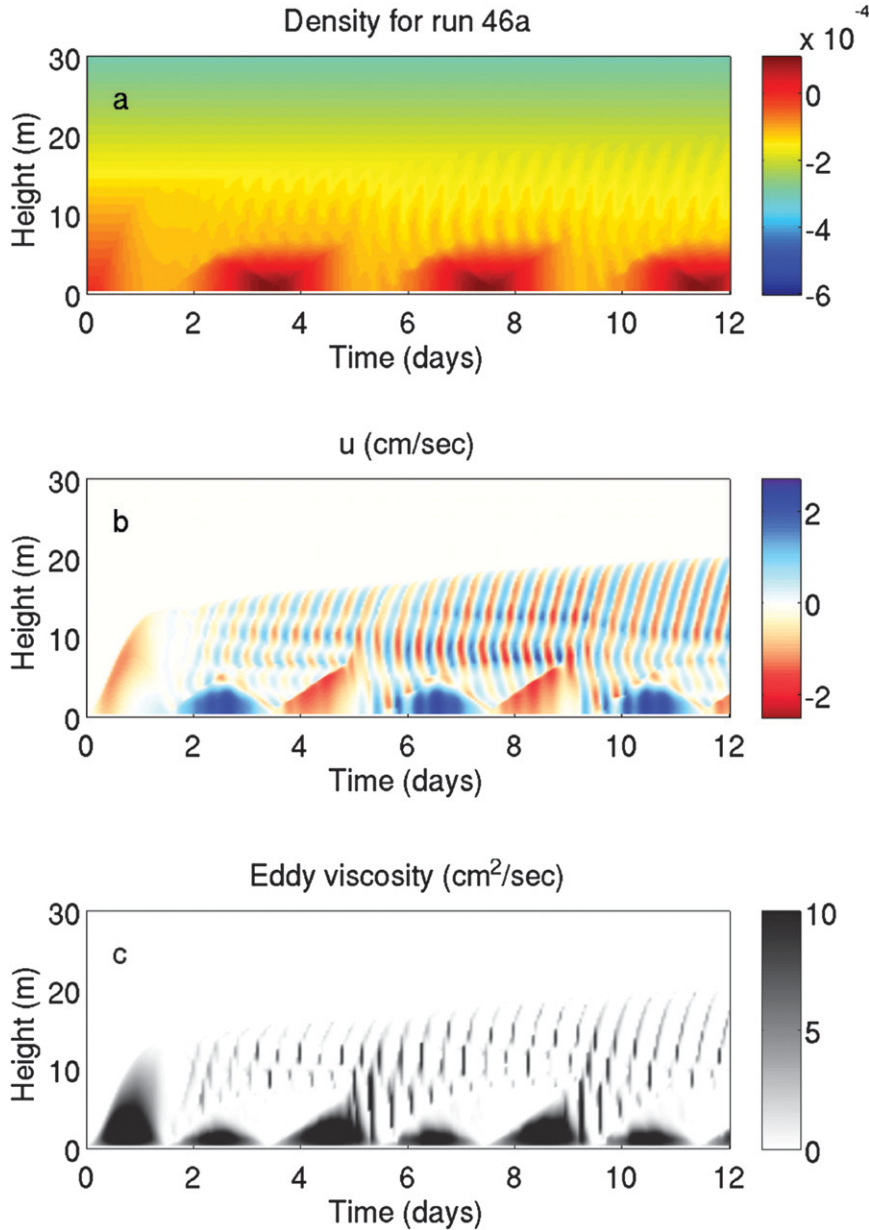
Density for run 46a

u (cm/sec)

Eddy viscosity (cm²/sec)

FIG. 6. As in Fig. 5, but for Results from model run 46a (4-day period, $s = 1.5$ and $\nu_0 = 20$ cm s^{-1}). Although the maximum value of eddy viscosity is about 26 cm^2 s^{-1}, the scale has been clipped so as to make the transitory eddy viscosity peaks in the upper boundary layer visible.

b. The capped regime boundary layer thickness

We seek an expression h^C for the boundary layer thickness in the capped oscillating regime where h_q and $h_{\rho\rho}$ are virtually equal. This regime appears in all our runs with superinertial forcing frequencies and in some subinertial cases with, for example, smaller s. Because the boundary layer is capped, we assume that its thickness is governed by a bulk Richardson number criterion (as is the case over a flat bottom). By analogy with the surface mixed layer (e.g., Niiler 1975), we expect that the boundary layer thickness is set at the moment when $\delta\rho/(\delta v)^2$ is a minimum.

At subinertial frequencies, the velocity jump δv is dominated by the cross-isobath component. If, for the purposes of illustration, we take the bottom Ekman transport to vary sinusoidally, then

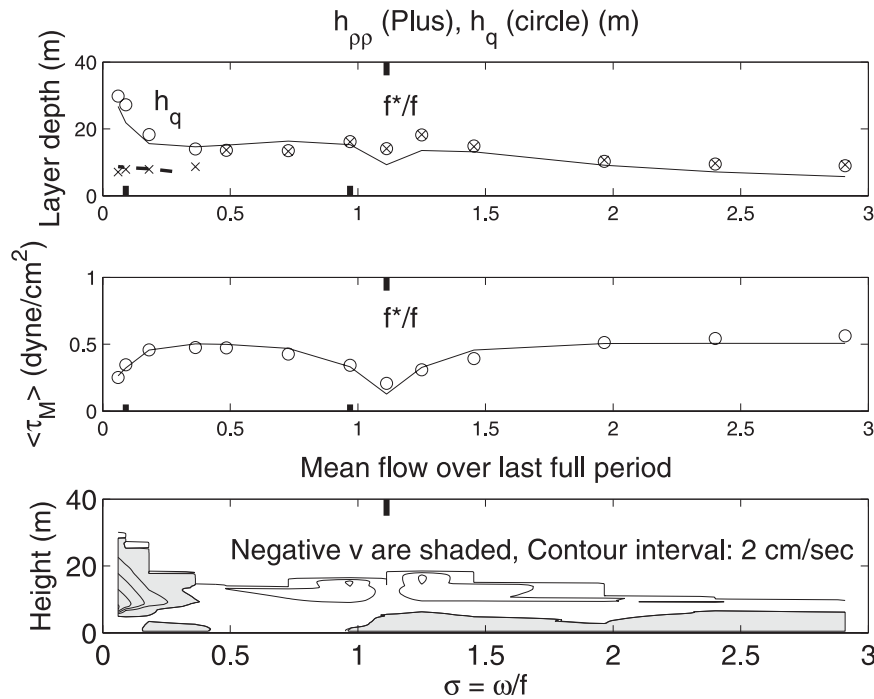$$\delta v \approx (\langle U_E \rangle / h^C) \sin(\omega t) \qquad (15a)$$

FIG. 7. Boundary layer behavior as a function of nondimensional frequency for $s = 0.5$ and $v_0 = 20$ cm s^{-1}: (top) boundary layer thickness. Computed results are shown by $\times$s ($h_{\rho\rho}$) or circles (h_q), and the solid lines represent analytical expressions for the outer boundary layer thickness (19) (capped regime) and (23) (divided regime). The dashed line is h^i, the fit for $h_{\rho\rho}$ [in (30a)]. (middle) Amplitude of the major-axis bottom stress (circles) with analytical expression (36) and (bottom) mean computed along-isobath velocity contoured as a function of height and $\sigma = \omega/f$ are shown. Negative values are shaded, and the contour interval is 2 cm s^{-1}.

and [by vertically integrating (1c)]

$$\delta\rho \approx -\frac{1}{2}h^C\rho_{Iz} + (\langle U_E\rangle/h^C)\alpha\rho_{Iz}\cos(\omega t), \quad (15b)$$

where the first term on the right-hand side of (15b) is due to entrainment and the second is due to upslope or downslope transport. It is then straightforward to minimize the ratio $\delta\rho/(\delta v)^2$ and show that its minimum occurs at roughly $t = \pi/(2\omega)$, the time when δv is a maximum, and where $\delta\rho$ is near its mean value, $\delta\rho \approx -h^C\rho_{Iz}/2$.

At superinertial frequencies, buoyancy advection is less important and again the second term on the right-hand side of (15b) is not important. Thus, the thickness of the capped boundary layer at any frequency is governed (now using the total scalar shear) by

$$R_b = \frac{gh^C\min[\delta\rho/(\delta v)^2]}{\rho_0}$$

$$\approx -\frac{1}{2}\frac{gh^{C^4}\rho_{Iz}}{[\rho_0(|\langle U_E\rangle|^2 + |\langle V_E\rangle|^2)]}. \quad (16)$$

We then repeat the approximations of section 3a but accounting for the sloping bottom. Specifically, the effective

inertial frequency changes from f to f^* and so the estimated unarrested friction velocity (13) over a sloping bottom is corrected to

$$\langle u^*\rangle = b_1 c_D^{1/2}v_0 F^*(\omega), \quad (17a)$$

where, generalizing (13b),

$$F^*(\omega) = \frac{1}{2}(2 - e^{-\lambda|f^* + \omega|/f^*} - e^{-\lambda|f^* - \omega|/f^*}). \quad (17b)$$

Using the depth-integrated form of (1), with sinusoidal stress variations,

$$\langle U_E\rangle \approx -\frac{f\langle u^*\rangle^2}{(f^{*2} - \omega'^2)} \quad \text{and} \quad (18a)$$

$$\langle V_E\rangle \approx -\frac{i\omega^*\langle u^*\rangle^2}{(f^{*2} - \omega'^2)}, \quad \text{with} \quad (18b)$$

$$\omega^* = \omega(1 - s^2/\sigma^2) \quad (18c)$$

and (16), we obtain (for small r)

$$h^C \approx c\langle u^*\rangle(f^2 + \omega^{*2})^{1/4}[(f^{*2} - \omega^2)^2 + 4r^2\omega^2]^{1/4}N^{-1/2}, \quad (19)$$

a form very similar to the flat-bottom case (11). The sloping bottom enters (19) through the s dependence in f^* and ω^* and through the expression for $\langle u^* \rangle$, which decreases near $\omega = \pm f^*$ (rather than $\pm f$). In the capped regime, computations show that the bottom stress is undiminished by buoyancy arrest (e.g., Figs. 3, 7, middle panels) so that the $\langle u^* \rangle$ value associated with the capped boundary layer thickness (17) likewise does not account for arrest.

A sequence of 17 numerical experiments in the capped regime (Table 2, runs where h_q and $h_{\rho\rho}$ agree to within about 1 m) shows that the flat-bottom values of b_1, c, and λ continue to hold. The correlation between h_q and h^C is 0.95 with an rms error of 2.4 m. The numerical results show a slight (about 1 m or less) sensitivity of h_q to initial conditions, and this sensitivity is an indication of the inherent scatter of these calculations. The analytical expression for capped boundary layer thickness (19) is shown in Fig. 3 (top) for $s < 0.3$ and in Fig. 7 (top) for $\sigma \geq 0.5$.

c. The divided boundary layer outer thickness

The outer boundary layer thickness in the divided regime is identified with h_q, the height where time-averaged turbulence vanishes. Stronger stratification is typically found in an inner boundary layer with $z < h_{\rho\rho}$, which is treated in section 4d. The numerical model runs (e.g., Figs. 6a,b) show that the outer boundary layer thickness is roughly set during the first downwelling-favorable excursion of the interior velocity, often before bottom stress is decreased by buoyancy arrest. That this thickness should not decrease after the first cycle is consistent with the idea that, once water is mixed vertically, there is no mechanism in this one-dimensional model to restore the stratification to its initial value. If the upwelling phase occurs before the downwelling, a shallow initial boundary layer is quickly erased during the subsequent growth of the thicker downwelling layer. After the initial thickening during the first cycle, the outer boundary layer still thickens gradually, at an ever-decreasing rate, evidently in conjunction with shear caused by the pseudoinertial oscillations.

During the initial downwelling phase, the weakly stratified boundary layer extends all the way to the bottom, and the entire layer is linearly stratified with the same gradient Richardson number Ri^D that characterizes the steady downwelling bottom boundary layer (Part I). Thus, if the outer boundary layer thickness is h^o (where superscript o stands for "outer"), the change in the vertical integral of ρ_E over the total depth of the boundary layer at the end of the first downwelling half cycle is

$$\Delta \int \rho_E \, dz = \rho_{Ez} \int (z - h^o) \, dz = \left(\frac{\rho_{Ez} h^{o^2}}{2} \right). \quad (20)$$

The boundary layer density gradient ρ_{Ez} is found by assuming a constant gradient Richardson number

$$Ri = -\frac{g(\rho_{Iz} + \rho_{Ez})}{(\rho_0 v_{Ez}^2)}$$

and geostrophy [(1a) with mixing and time dependence neglected] in the outer boundary layer. We obtain

$$\rho_{Ez} = -\frac{\rho_{Iz}(-1 + \Gamma)}{(Ri s^2)}$$

$$= -\rho_{Iz}/\Gamma \quad \text{and} \quad (21a)$$

$$\Gamma = \frac{[1 + (1 + 4Ri^D s^2)^{1/2}]}{2}, \quad (21b)$$

where the positive root is chosen in the quadratic solution for ρ_{Ez} so that stratification is weaker in the boundary layer. The second equality in (21a) comes simply from algebraic manipulation of the first equality. Empirically, we find $Ri^D = 0.7$, as in Part I.

By integrating (1c) vertically (from the bottom to a height greater than the boundary layer thickness) and temporally (over a quarter cycle), we find that the time change in vertically integrated density is

$$\Delta \int \rho_E \, dz + \langle U_E \rangle \alpha \rho_{Iz}/\omega = 0, \quad (22)$$

where the boundary layer transport amplitude $\langle U_E \rangle$ is given by (18a) (it is reasonable to drop the r^2 term in the expression for $\langle U_E \rangle$, because it is only important for frequencies near the pseudoinertial and the divided regime generally occurs at subinertial frequencies; see section 4e). The applicable u^* amplitude here is given by (17), which accounts for the shift in effective inertial frequency but not for buoyancy arrest. That is, the change in integrated boundary layer density is effected by the initial, unarrested Ekman advection so that, from (20), (21a), and (22),

$$h^{o^2} = -\frac{2\langle U_E \rangle \alpha \Gamma}{\omega} = \frac{2\langle u^* \rangle^2 f \alpha \Gamma}{[\omega(f^{*2} - \omega^2)]}. \quad (23)$$

The Ekman transport formulation used here assumes that bottom stress has not been reduced by buoyancy arrest; however, this is not always the case. If bottom stress, hence Ekman transport, is arrested, the downslope excursion in the boundary layer is constrained so that the boundary layer thickness remains bounded as $\omega \to 0$. Thus, we require that the outer boundary layer can never reach a thickness greater than that of the steady limit, where bottom stress is completely arrested (Part I):
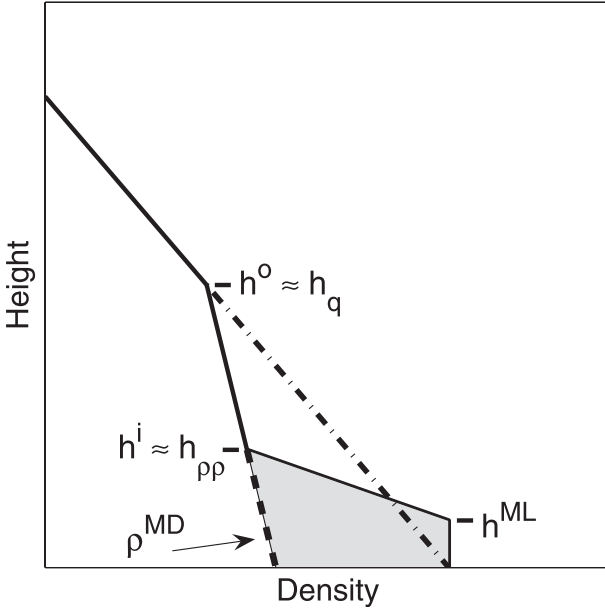
FIG. 8. Schematic of a typical divided bottom boundary layer mean density structure.

$$h^o \le h^o_{\max} = \frac{|v_0|\Gamma}{(sN)}. \tag{24}$$

Expressions (23) and (24) were evaluated using 36 divided regime numerical model runs (delineated using the criterion of section 4e) and were found to agree with h_q with a correlation of 0.95 and an rms difference of 3.2 m (out of an h_q range of roughly 32 m). Expressions (23) and (24) were used to generate the solid lines in Figs. 3 and 7 (top panels) for $s > 0.35$ and $\sigma < 0.5$, respectively.

d. The divided boundary layer inner thickness

The typical structure of the time-mean bottom boundary layer in the divided regime is sketched in Fig. 8 (solid line), which can be compared to an actual model run in Fig. 4 (dashed line). The outer part of the mean boundary layer is weakly stratified (as described in section 4c), but the inner part of the boundary layer is more strongly stratified and often has a distinct bottom mixed layer. During the maximal downwelling excursion of the Ekman transport, the inner boundary layer vanishes, and the near-bottom density is given by $\rho^{MD}(z)$, the dashed line in Fig. 8. At this moment, the vertically integrated density change (relative to the mean density), associated with downslope transport, must be [from (22)] associated with boundary layer advection,

$$\Delta \int \rho_E \, dz = \frac{\langle U_E^A \rangle \alpha \rho_{Iz}}{\omega}, \tag{25}$$

where the integral represents the shaded area on Fig. 8. Here, $\langle U_E^A \rangle$ is the Ekman transport amplitude, where its reduction resulting from buoyancy arrest has now been accounted for [the expression for $\langle U_E \rangle$ in Eq. (18) does not account for buoyancy arrest]. In contrast, during the maximal upwelling excursion, the strongly stratified inner boundary layer has a thickness of $h_{\rho\rho} < h_q$, and the bottom density substantially exceeds the initial density (that obtained by extrapolating the interior density gradient toward the bottom; the dashed–dotted curve in Fig. 8). Averaged over a cycle, the bottom stress vanishes to a good approximation, so we take the bottom geostrophic mean velocity to be zero. Geostrophy [(1a) time averaged and neglecting the stress term] then implies that the time-mean boundary layer density $\rho_E \approx 0$ at the bottom. Also, averaged over a cycle, there is a well-defined bottom mixed layer of thickness h^{ML}. We use this information to create an analytical estimate h^i for the inner boundary layer thickness $h_{\rho\rho}$.

The finite stratification in the outer part of the inner layer (i.e., where $h^{ML} < z < h_{\rho\rho}$) is found to be governed, over a time average, by the same gradient Richardson number $Ri^U = 0.4$ that applies in the steady upwelling case (Part I). Thus, the difference in density between heights h^{ML} and h^i is simply

$$\rho(z = h^{ML}) - \rho(z = h^i) = -(h^i - h^{ML})\rho_z$$
$$= -(h^i - h^{ML})\rho_{Iz}(1 + \Lambda^{-1}), \tag{26a}$$

where

$$\Lambda = \frac{[-1 + (1 + 4Ri^U s^2)^{1/2}]}{2}. \tag{26b}$$

The expression for ρ_{Ez} used in (26) is obtained by following the derivation of (21a), except that the negative root is taken in the quadratic solution so that stratification is enhanced in the boundary layer. The constraint that $\rho_E \approx 0$ at the bottom (equivalent, through geostrophy, with there being no mean flow at the bottom) allows estimation of the terms in (25): specifically,

$$\Delta \int \rho_E \, dz \approx \frac{1}{2}[\delta\rho(z = 0) + \delta\rho(z = h^{ML})]h^{ML}$$
$$+ \frac{1}{2}(h^i - h^{ML})\delta\rho(z = h^{ML}), \tag{27}$$

where (using the diagram and knowledge of density gradients that are governed by constant gradient Richardson numbers Ri^D and Ri^U in the inner and outer boundary layers)

$$\delta\rho(z = 0) = \rho(z = 0) - \rho^{MD}(z = 0) = -h^o \rho_{Iz}/\Gamma \quad \text{and}$$
$$\tag{28a}$$

$$\delta\rho(z = h^{\mathrm{ML}}) = \rho(z = h^{\mathrm{ML}}) - \rho^{\mathrm{MD}}(z = h^{\mathrm{ML}})$$

$$= -(h^i - h^{\mathrm{ML}})\rho_{\mathrm{Iz}}/\Gamma - h^{\mathrm{ML}}\rho_{\mathrm{Iz}}. \qquad (28b)$$

We now express the actual (buoyancy arrest–decreased) bottom Ekman transport in terms of the unarrested transport as

$$\langle U_E^A \rangle = \theta \langle U_E \rangle \qquad (29a)$$

or, equivalently,

$$\langle u*^A \rangle = \theta^{1/2}\langle u* \rangle. \qquad (29b)$$

We add superscript A to the symbols U_E and $u*$ as a reminder that these quantities have been reduced by buoyancy arrest. The functional form for θ is treated in section 4f. It is then straightforward to use (25)–(29) to obtain a quadratic expression for h^i. For $s < 0.5$, it is a reasonable approximation to take $\Lambda \ll 1$, in which case

$$h^i \approx \frac{1}{2}h^o(\theta + \Lambda/\Gamma) \quad \text{and} \qquad (30a)$$

$$h^{\mathrm{ML}} \approx h^i - h^o\Lambda/\Gamma. \qquad (30b)$$

We also impose the constraint that $h^{\mathrm{ML}} \geq 0$. Note that, for $\Lambda \to 0$ (small s), either (26) or (30b) imply that $h^{\mathrm{ML}} = h^i$: that is, the inner boundary layer becomes a capped mixed layer. In practice, the greatly simplified expressions in (30) work as well as a more complete solution to (25)–(29), even for $s > 1$.

The expressions (30) were evaluated against 36 divided regime boundary layer calculations, where h^i was compared to $h_{\rho\rho}$ and h^{ML} to a bottom mixed layer thickness. For this comparison, the model bottom mixed layer was defined as the height at which density changes 2×10^{-8} gm cm^{-3} relative to the bottom density. Expression (30a) agrees with $h_{\rho\rho}$ to an rms error of 1.9 m and with a correlation of 0.84. The comparable numbers for the analytical mixed layer estimate (30b) are 2.8 m and 0.78. Expression (30a) was used to generate the dashed lines in Figs. 3 and 7 (top panels).

e. Boundary layer regimes

The transition between the capped and divided boundary layer regimes occurs when the stable cap resulting from entrainment is overcome by gravitational instability because of the downslope Ekman layer advection. Once this occurs, an outer boundary layer with constant gradient Richardson number Ri^D forms and reaches height h^o. When the bottom Ekman transport returns to the upslope direction, a transitory inner boundary layer of thickness h^i forms, and this is reflected in the mean over a cycle (Fig. 8).
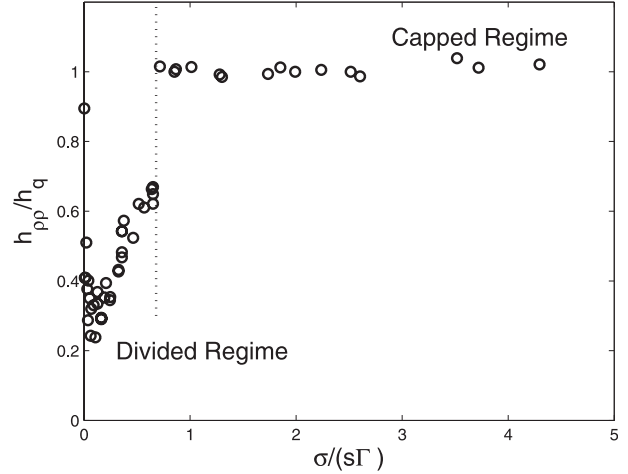

FIG. 9. Numerical model estimates of the ratio of inner to outer boundary layer thickness ($h_{\rho\rho}/h_q$) as a function of $\sigma/(s\Gamma)$. The dotted vertical line, dividing the two regimes, occurs at $\sigma/(s\Gamma) = 0.68$.

The transition between the capped and divided regimes occurs when the capped and divided outer boundary layer thicknesses become equal: that is, when

$$h^o = h^C \qquad (31a)$$

so that, from (19) under the low-frequency assumption that $f*^2 \gg \omega*^2$, and (23),

$$\frac{2\langle U_E \rangle \alpha\Gamma}{\omega} = \frac{c^2\langle U_E \rangle}{N}. \qquad (31b)$$

Thus, the transition is expected to occur when

$$\frac{\omega}{(\alpha N\Gamma)} = \frac{\sigma}{(s\Gamma)} = \frac{2}{c^2}. \qquad (31c)$$

The regime transition is demonstrated by Fig. 9, which shows the ratio $h_{\rho\rho}/h_q$ as a function of $\sigma/(s\Gamma)$. This distinguishes the regimes because, in the capped case, the two boundary layer definitions coincide but, in the divided case, the two layer definitions differ sharply (e.g., Figs. 3, 7). We find that the regime transition occurs for $\sigma/(s\Gamma)$ near 0.68, a somewhat larger value than the 0.41 that would be expected using the established value of $c = 2.2$ in (31c). We note that the expression for h^C in (19) is an approximation, where the corrections enter at order $(s/\sigma)^2$: that is, they grow as the capped–divided transition is approached. It thus seems possible that this inconsistency in estimating the actual transition point is ultimately related to the approximation that the capped boundary layer density jump is unaffected by advection.

f. Bottom stress

Time series of model bottom stress show that, after the first cycle of a model run, the stress reaches a periodic

pattern that is distinctly symmetric between the up-welling and downwelling phases. No substantial mean bottom stress is ever detected. In the capped boundary layer regime, there is no observable reduction in bottom stress relative to (17); however, in the divided regime, the friction velocity amplitude is reduced, to varying degrees, relative to (17). The reduction is consistent with buoyancy arrest reducing the bottom stress.

We now develop a scaling for the bottom stress reduction. Because fluctuating buoyancy arrest is found to occur at frequencies lower than the pseudoinertial, we begin with the depth-integrated (over the total boundary layer thickness), low-frequency filtered versions of (1):

$$-fV_E = -\frac{g\alpha \int \rho_E \, dz}{\rho_0}, \tag{32a}$$

$$V_{Et} + fU_E = -\frac{\tau^y}{\rho_0}, \quad \text{and} \tag{32b}$$

$$\int \rho_{Et} \, dz + U_E \alpha \rho_{Iz} = 0. \tag{32c}$$

The rationale for these equations is that they remove near-inertial oscillations but that they retain the physics of arrest [see Part I; it is worth noting that if Eq. (32) is taken to represent flow averaged over a period, it is straightforward to show that, in a steady state, with all time derivatives equal to zero, there can be no mean along-isobath stress]. The system (32) is readily reduced to the single equation,

$$\left[\frac{(1 + s^2)}{s^2}\right] V_{Et} = -\frac{\tau^y}{\rho_0}. \tag{33}$$

The magnitude of the along-isobath boundary layer transport V_E is expected to increase if the interior flow amplitude v_0 increases, and it also ought to increase as the boundary layer becomes thicker if $v_E = O(v_0)$. Thus, we conjecture that the magnitude of V_{Et} is given by

$$|V_{Et}^A| = \Xi \omega v_0 h^o, \tag{34}$$

where Ξ is a constant and the boundary layer thickness h^o is given by (23). Recall that h^o generally depends on $\langle u* \rangle$, the stress amplitude before buoyancy arrest occurs. The stress amplitude with arrest is, from (17a) and (29b),

$$\frac{\langle \tau^y \rangle}{\rho_0} = \langle u^{*A} \rangle^2 = [b_1 c_D^{1/2} v_0 F*(\omega)]^2 \theta. \tag{35}$$

Because the low-frequency approximation avoids the near-inertial frequency, it is also consistent here to take $F* \approx 1$. Using (23), (34), and (35) in (33) yields

$$\theta \approx \Xi (b_1 s)^{-1} \left[\frac{2\Gamma\sigma(1 + s^2)}{(ds)}\right]^{1/2} \equiv \Xi\zeta \le 1, \tag{36}$$
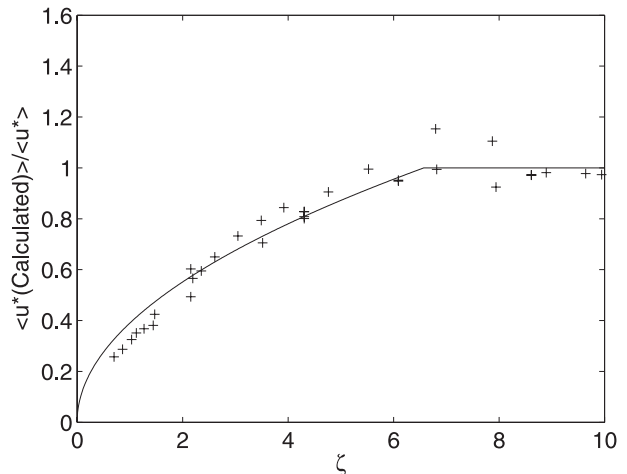

FIG. 10. Numerical model $u*$ amplitude normalized by the un-arrested $u*$ amplitude estimated using (17). The horizontal axis is the arrest parameter $\zeta = (b_1 s)^{-1}[2\Gamma\sigma(1 + s^2)/(ds)]^{1/2}$. The solid line is the analytical expression for arrest $\langle u^{*A} \rangle = \theta^{1/2} \langle u* \rangle$, where θ is given by (36); that is, $|\theta| \approx 0.15\zeta \le 1$.

where we have added the constraint ($\theta \le 1$) that buoyancy arrest cannot enhance bottom stress. This form can then be used in (29b) or (35):

$$\langle u^{*A} \rangle = \theta^{1/2} \langle u* \rangle = b_1 c_D^{1/2} v_0 F*(\omega)\theta^{1/2}. \tag{37}$$

The functional form (36) is evaluated using all of the sloping-bottom runs (Table 2), yielding $\Xi = 0.15$, an rms error for $\langle u^{*A} \rangle$ of 0.05 cm s^{-1}, and a correlation of 0.98 (Fig. 10). Expression (36) was used to generate the solid lines in the middle panels of Figs. 3 and 7. The scaling (36) could also have been obtained simply by making assumption (34) with the arrested form of (18b) and assuming that $\sigma^2/s^2 \ll 1$. The present derivation serves to highlight the nearly geostrophic physics.

g. Rectified flow

Rectified flow having magnitude up to 60% of the interior amplitude occurs in the model runs (e.g., Figs. 3, 4, 7, 11), but the mean flow is in different directions at higher and lower frequencies (Fig. 7). Specifically, in the capped regime, mean flow is positive in the upper part of the boundary layer but very weakly negative or zero below (e.g., the solid curves in Fig. 11). In the divided regime, there is a negative mean flow peaking near $z = h_{\rho\rho}$ and then tapering off in the outer part of the boundary layer (dashed curves in Fig. 11). The two regimes are treated separately here.

1) CAPPED REGIME RECTIFICATION

In the capped regime (e.g., Fig. 7; $\sigma > 0.5$), where either frequencies are relatively high or s is relatively
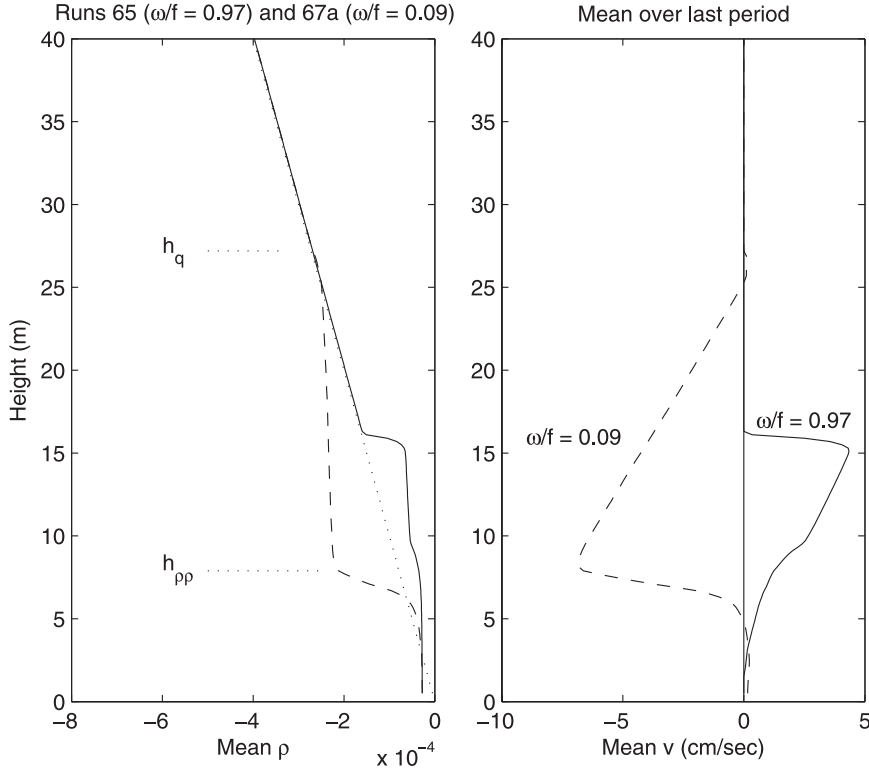
FIG. 11. Mean (over the last forcing period) conditions for $s = 0.5$, $v_0 = 20$ cm s^{-1}, and $\sigma = \omega/f = 0.97$ (run 65: solid line) or $\sigma = \omega/f = 0.09$ (run 67a: dashed line). These frequencies are flagged by the solid bars in Fig. 7 (top). (left) total density (with the dotted line showing the undisturbed, initial density) and (right) mean velocity are shown. The heights of vanishing turbulence h_q and of maximum density gradient $h_{\rho\rho}$ are shown for run 67a (dashed line) in (left).

small, cross-isobath density transport is rather modest. At high frequencies, little net water is exchanged up or down the slope, because the cross-slope particle excursion [proportional to $U_E/(h\omega)$] is relatively small. At lower frequencies but with a modest bottom slope, even substantial cross-isobath displacements do not yield large density changes. Under these conditions, density in the bottom boundary layer is governed more by vertical entrainment than by lateral advection. The total density (sum of boundary layer and interior components) within this sharply capped boundary layer is homogeneous and equal to the initial density averaged over the thickness of the layer.

If lateral advection can thus be ignored in the buoyancy balance (as in section 4b), the boundary layer component of mean density at the top of the layer, $z \approx h^C$, is about

$$\overline{\rho}_E(z = h^C) = -0.5h^C\rho_{Iz}. \qquad (38)$$

Further, we find that, in the upper portion of the boundary layer, the mean turbulent stress divergence terms

are negligible, so the mean along-isobath flow there is geostrophic. Thus [from (1a) with $A = 0$], the geostrophic component of period-averaged along-isobath flow v_E at the top of the bottom boundary layer is

$$\overline{v}_E(z = h^C) = \frac{g\alpha\overline{\rho}_E(z = h^C)}{(f\rho_0)} = -\frac{0.5g\alpha h^C\rho_{Iz}}{(f\rho_0)} = 0.5sNh^C > 0$$
$$= 0.5c\langle u*\rangle sN^{1/2}(f^2 + \omega*^2)^{1/4}$$
$$\times [(f*^2 - \omega^2)^2 + 4r^2\omega^2]^{-1/4}. \qquad (39)$$

This is the maximum (as a function of height) possible geostrophic velocity for this idealization, because it occurs where the density perturbation is maximal. In the lower half of the capped boundary layer, the mean velocity term becomes negligible, whereas the stress gradient terms become more important. The capped mean flow structure in Fig. 11 (right, solid line) can thus be rationalized in light of the importance of geostrophy versus turbulent stress divergence. Comparing (39) to the maximum rectified flow for all 17 capped regime numerical model runs shows agreement to an rms error of about

1.4 cm s^{-1} (correlation 0.91), compared to a 10 cm s^{-1} mean flow range.

A substantial positive (toward the right as one looks from shallower water into deeper water in the Northern Hemisphere) mean flow might be expected with strong tides and a stratified interior. This rectification differs from traditional tidal rectification (e.g., Loder 1980) in that the mean flow depends critically on the presence of a stratified interior and because the mean flow is distinctly confined vertically.

2) DIVIDED REGIME RECTIFICATION

During divided regime conditions, the outer boundary layer (where $h_q > z > h_{\rho\rho}$) is weakly stratified compared to the interior and not strongly turbulent on average. The associated mean (over an interior velocity period) along-isobath flow in the outer region is in geostrophic balance [(1a) with $A = 0$] and has a constant gradient Richardson number, Ri^D. Thus,

$$\bar{v}_{\mathrm{E}z} = \frac{f^{-1}g\alpha\bar{\rho}_{\mathrm{E}z}}{\rho_0} \tag{40a}$$

and, using (21),

$$\bar{v}_{\mathrm{E}z} = \frac{sN}{\Gamma}. \tag{40b}$$

Combining these, we obtain, for $h^o > z > h^i$,

$$\bar{v}_E = \left(\frac{sN}{\Gamma}\right)(z - h^o). \tag{41}$$

The rectified flow is negative and the maximum magnitude occurs at the lower edge of the outer boundary layer, $z = h_{\rho\rho} \approx h^i$. If there is a bottom mixed layer for $z < h^i$, then there is a weaker positive mean flow similar to that in the capped case (earlier). Using (41) to estimate modeled extreme (as a function of height) negative mean along-isobath flow yields an rms difference of 4.3 cm s^{-1} (correlation of 0.81) compared to a range of numerical model mean flows of 17 cm s^{-1}.

5. Broadband forcing

In nature, current fluctuations are rarely monotonic, as assumed up to this point. Rather, variations occur over a broad frequency range. The time-dependent buoyancy arrest problem involves nonlinearities through the variable turbulence (hence boundary layer thickness) and through the quadratic stress form so that it is reasonable to ask whether results up to this point change substantially in response to more realistic broadband forcing.

We address this question by solving (1) numerically, starting with a constant initial stratification ($N = 1.3 \times 10^{-2}$ s^{-1}, $f = 0.95 \times 10^{-4}$ s^{-1}, and $c_D = 2.9 \times 10^{-3}$) and using an observed middepth hourly time series of continental shelf along-isobath currents for v_I. Each run lasted 100 days. Time series from the Georges Bank southern flank (e.g., Brink et al. 2009) were used for most runs. Because these time series were dominated by energetic M$_2$ tides (amplitude of order 25 cm s^{-1}), midshelf (C3) current records from the central Californian Coastal Ocean Dynamics Experiment (CODE) area (e.g., Winant et al. 1987) were used to provide contrasting time series with less energetic tidal currents. Finally, each model run was repeated with three bottom slopes: $\alpha = 0$ ($s = 0$), 0.000 75 ($s = 0.11$), and 0.003 75 ($s = 0.53$), the nonzero bottom slope choices being representative of the U.S. Mid-Atlantic Bight shelf (or Georges Bank) and of the U.S. Northern California shelf. Runs were done in various configurations (e.g., with and without mean interior along-isobath currents included), using a reversed mean current (i.e., replacing the observed mean current with an equal and opposite mean), using a linearized bottom stress, and using low-pass filtered (tides removed) time series.

All model runs are strikingly similar in two regards. One is that arrest of the steady flow component occurs over roughly the time scales expected from Part I, so the later parts of all sloping-bottom model time series have no mean bottom stress. Second, in all model runs, the bottom boundary layer continues to thicken with time. In the flat-bottom runs, the boundary layer deepens only very slowly after the first 20 days (e.g., about 10% over about 80 days). For the model runs with a sloping bottom, the boundary layer thickness (as defined by h_q) keeps increasing with each new extreme of downslope excursion in the bottom boundary layer. Because there is nothing in the model system (1) that can act to restore the initial stratification, there is no way for the outer boundary layer to become less thick. The inner boundary layer presents a more complex time history, because it comes and goes as upslope flow comes and goes.

Coupling between frequencies occurs through the nonlinear form of the bottom stress (3), which assures that, if speeds are decreased in one frequency band (because of arrest), the bottom stress is decreased at all frequencies. This stress reduction is explored by considering model time series of bottom stress and interior along-isobath velocity. Both time series are Fourier analyzed (using standard fast Fourier transform techniques) into individual frequencies; then the ratio

$$R(\omega) = \frac{\tau^y}{(\rho_0 b_1^2 c_D |v_I| v_I)} \tag{42}$$
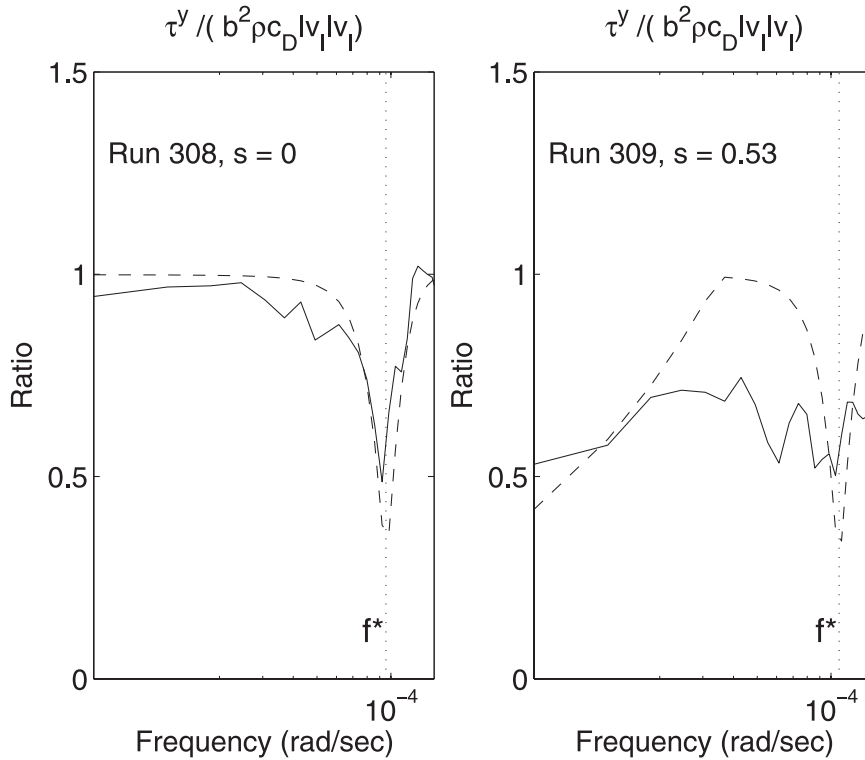
$$\tau^y / (b^2 \rho c_D |v_I| v_I)$$

FIG. 12. Stress ratio (42) as a function of frequency for model runs driven by observed Georges Bank 30-m along-isobath currents: run (left) 308 and (right) 309. The solid line is for results calculated directly from Fourier-analyzed model output time series, and the dashed line is the analytical expression (43), which is only valid to the extent that results at different frequencies can be linearly superimposed.

is computed frequency by frequency. If the different frequencies superimpose linearly, then one might expect, from (17) and (37), that

$$R(\omega) = \theta F^*(\omega)^2. \qquad (43)$$

Results for two model runs (with hourly Georges Bank currents, $s = 0$ and $s = 0.53$) summarize the results (Fig. 12). For a flat-bottom case with no arrest (left panel), the stress ratio R computed directly from the model time series (solid line) agrees fairly well with the analytical form (43), indicating that stress at individual frequencies can be treated independently. On the other hand, for $s = 0.53$ (right panel), actual model bottom stress is reduced relative to (43) at nearly all frequencies (i.e., stress even decreases at frequencies well above the inertial). A similar model run with $s = 0.11$ (not shown) gives a more modest stress reduction but still over all frequencies. These results are typical of all model runs with quadratic bottom stress, in that stress reduction occurs over a frequency range much larger than would be expected from (43). In contrast, model runs with a linearized bottom stress (which still allows arrest but does not allow frequency coupling through the bottom boundary condition)

are much more consistent with (43) holding frequency by frequency. For example, a run similar to that of the right panel in Fig. 12 ($s = 0.53$), but with linearized bottom stress, largely eliminates the stress decrease relative to (43) for periods shorter than about 1.5 days (frequencies greater than 5×10^{-5} s^{-1}). Because linearizing the bottom stress appears to make (43) become valid, it seems likely that any coupling associated with mixing is less important for explaining the failure of (43). Thus, over a sloping bottom, buoyancy arrest plus quadratic bottom drag combine to weaken stress at all frequencies.

6. Conclusions

In response to oscillating interior along-isobath flow in a stratified ocean with a sloping bottom, the bottom boundary layer takes on one of two general structures. For small $s = \alpha N/f$ or large $\sigma = \omega/f$, there is a bottom mixed layer with a sharply defined density cap. The layer's thickness decreases slightly as s increases (Fig. 3; Table 3), and it approaches the flat-bottom thickness as s becomes small. This well-mixed case, which is qualitatively similar to results with a flat bottom, is referred to

TABLE 3. Summary of fluctuating boundary layer thickness formulae.

Case	Boundary layer thickness
Capped	$h^C = c\langle u^*\rangle(f^2 + \omega^{*2})^{1/4}[(f^{*2} - \omega^2)^2 + 4r^2\omega^2]^{-1/4}N^{-1/2}$
Divided (outer)	$(h^o)^2 = 2\langle u^*\rangle^2 fa\Gamma/\omega(f^{*2} - \omega^2)$
	$h^o_{max} = \|v_0\|\Gamma/sN$
	$\Gamma(s) = \frac{1}{2}[1 + (1 + 4\mathrm{Ri}^D s^2)^{1/2}]$
Divided (inner)	$h^i \approx \frac{1}{2}h^o(\theta + \Lambda/\Gamma) \quad \Lambda(s) = \frac{1}{2}[-1 + (1 + 4\mathrm{Ri}^U s^2)^{1/2}]$

as the capped regime. For large enough s or small enough σ, the boundary layer structure, averaged over a forcing period, changes dramatically so that there is a weakly stratified outer boundary layer reaching height h_q (approximated by h^o) above the bottom and a strongly stratified inner boundary layer (Table 3, the divided regime). In practice, we find that the transition between the capped and divided regimes occurs when $\sigma/(s\Gamma) \approx 0.68$. This criterion effectively defines what is meant by small or large s or σ.

Buoyancy arrest (i.e., the neutralization of bottom stress) comes into play only in the divided regime, and the decrease in stress amplitude is governed by (36). Buoyancy arrest becomes more important for lower frequencies (small σ) and larger drag (larger d), but the strongest dependence is on the slope Burger number s. It is straightforward to use (36) to estimate when one might expect to observe buoyancy arrest for fluctuating flows in the ocean. The inequality implies that there is no arrest at all if $\zeta < 6.6$. Consider the representative examples of summertime continental shelf conditions in the Mid-Atlantic Bight and off the coast of Oregon. In both cases, $d \approx 0.3$ and $f \approx 1 \times 10^{-4}$ s^{-1}; however, for the Mid-Atlantic Bight $s \approx 0.1$ and for Oregon $s \approx 0.5$. The arrest cutoff periods differ dramatically: in the Mid-Atlantic Bight, arrest only occurs for periods longer than about 27 days, whereas off Oregon arrest begins at period of about 1.5 days. Further, for Oregon, the bottom stress amplitude is expected to fall to half its unarrested value at a period of about 6 days (the comparable number is 108 days for the Mid-Atlantic Bight). The strong s dependence in (36) thus suggests that, on the gently sloping Mid-Atlantic Bight shelf, buoyancy arrest is negligible for most fluctuating flows (because stratification is absent during the winter) but that, on the Oregon shelf, arrest is important for variations having "weather band" and longer time scales.

Even though the asymmetry of upwelling and downwelling Ekman transport does not induce a mean bottom stress, mean flows do develop in the bottom boundary layer. In the capped regime (i.e., for higher frequencies; $\sigma > 0.5$ in Fig. 7, or see Fig. 11), a bottom mixed layer

always develops, and its density is governed primarily by entrainment. In this case, a positive mean along-isobath flow develops. This flow is approximately in geostrophic balance in the upper part of the bottom mixed layer; however, as the bottom is approached, dissipative effects become important and negate any rectification. In the divided regime (i.e., for lower frequencies; $\sigma < 0.3$ in Fig. 7), a strong (up to order 10 cm s^{-1}) negative, geostrophically balanced, along-isobath mean flow develops above the bottom mixed layer but within the outer boundary layer.

Uncertainty remains as to how well these present results would apply to the actual three-dimensional ocean. For example, in our model, the boundary layer thickness can only increase with time. However, in nature (e.g., Lentz and Trowbridge 1991; Perlin et al. 2007), actual boundary layer thickness both increases and decreases with time, evidently as a result of interior advective processes that cannot be included in our nearly one-dimensional model. This question of the enduring versus transitory nature of the boundary layer thickness reflects on many of our results, including mean flow generation and stress modification. Our present results, then, should probably be taken as realistic only over time scales less than those over which stratification is reestablished by lateral advection.

REFERENCES

Brink, K. H., and S. J. Lentz, 2010: Buoyancy arrest and bottom Ekman transport: Part I. Steady flow. *J. Phys. Oceanogr.,* **40,** 621–635.

——, R. C. Beardsley, R. Limeburner, J. D. Irish, and M. Caruso, 2009: Long-term moored array measurements of currents and hydrography over Georges Bank: 1994–1999. *Prog. Oceanogr.,* **82,** 191–223, doi:10.1016/j.pocean.2009.07.004.

Chapman, D. C., 2000a: A numerical study of the adjustment of a narrow stratified current over a sloping bottom. *J. Phys. Oceanogr.,* **30,** 2927–2940.

——, 2000b: Boundary layer control of buoyant coastal currents and the establishment of a shelfbreak front. *J. Phys. Oceanogr.,* **30,** 2941–2955.

——, and S. J. Lentz, 1994: Trapping of a coastal density front by the bottom boundary layer. *J. Phys. Oceanogr.,* **24,** 1464–1479.

Garrett, C., P. MacCready, and P. B. Rhines, 1993: Boundary mixing and arrested Ekman layers: Rotating stratified flow near a sloping bottom. *Annu. Rev. Fluid Mech.,* **25,** 291–324.

Lentz, S. J., and J. H. Trowbridge, 1991: The bottom boundary layer over the northern California shelf. *J. Phys. Oceanogr.,* **21,** 1186–1201.

Loder, J., 1980: Topographic rectification of tidal currents on the sides of Georges Bank. *J. Phys. Oceanogr.,* **10,** 1399–1416.

MacCready, P., and P. B. Rhines, 1991: Buoyant inhibition of Ekman transport on a slope and its effect on stratified spin-up. *J. Fluid Mech.,* **223,** 631–661.

——, and ——, 1993: Slippery bottom boundary layers on a slope. *J. Phys. Oceanogr.,* **23,** 5–22.

Middleton, J. F., and D. Ramsden, 1996: The evolution of the bottom boundary layer on the sloping continental shelf: A numerical study. *J. Geophys. Res.,* **101** (C8), 18 061–18 077.

Niiler, P. P., 1975: Deepening of the wind-mixed layer. *J. Mar. Res.,* **33,** 405–422.

Perlin, A., J. N. Moum, and J. M. Klymak, 2005: Response of the bottom boundary layer over a sloping shelf to variations in alongshore wind. *J. Geophys. Res.,* **110,** C10S09, doi:10.1029/2004JC002500.

——, ——, ——, M. D. Levine, T. Boyd, and P. M. Kosro, 2007: Organization of stratification, turbulence, and veering in bottom Ekman layers. *J. Geophys. Res.,* **112,** C05S90, doi:10.1029/2004JC002641.

Pollard, R. T., P. B. Rhines, and R. O. R. Y. Thompson, 1973: The deepening of the wind-mixed layer. *J. Geophys. Fluid Dyn.,* **3,** 381–404.

Ramsden, D., 1995a: Response of an oceanic bottom boundary layer on a slope to the interior flow. Part I: Time-independent interior flow. *J. Phys. Oceanogr.,* **25,** 1672–1687.

——, 1995b: Response of an oceanic bottom boundary layer on a slope to the interior flow. Part II: Time-dependent interior flow. *J. Phys. Oceanogr.,* **25,** 1688–1695.

Romanou, A., and G. L. Weatherly, 2001: Numerical simulations of buoyant Ekman layers in the presence of variable stratification. Part I: Constant interior forcing. *J. Phys. Oceanogr.,* **31,** 3096–3120.

——, and ——, 2004: Numerical simulations of buoyant Ekman layers. Part II: Rectification in zero-mean, time-dependent forcing, and feedback on the interior flow. *J. Phys. Oceanogr.,* **34,** 1050–1066.

Thompson, R. O. R. Y., 1973: Stratified Ekman boundary layer models. *Geophys. Fluid Dyn.,* **5,** 201–210.

Trowbridge, J. H., and S. J. Lentz, 1991: Asymmetric behavior of an oceanic boundary layer above a sloping bottom. *J. Phys. Oceanogr.,* **21,** 1171–1185.

Weatherly, G. L., and P. J. Martin, 1978: On the structure and dynamics of the oceanic bottom boundary layer. *J. Phys. Oceanogr.,* **8,** 557–570.

Wijesekera, H. W., J. S. Allen, and P. A. Newberger, 2003: A modeling study of turbulent mixing over the continental shelf: Comparison of turbulent closure schemes. *J. Geophys. Res.,* **108,** 3103, doi:10.1029/2001JC001234.

Winant, C. D., R. C. Beardsley, and R. E. Davis, 1987: Moored wind, temperature, and current observations made during Coastal Ocean Dynamics Experiments 1 and 2 over the northern California continental shelf and upper slope. *J. Geophys. Res.,* **92,** 1569–1605.